RESEARCH ARTICLE

ADVANCED OPTICAL MATERIALS
www.advopticalmat.de

High-Performance UV Photodetector via Energy Band Engineering and LSPR-Enhanced Pyro-Phototronic Effect in Au Decorated 2D-PbI_2/1D-ZnO Heterojunction

Xuemei Zheng, Mengji Dong, Qi Li, Yanli Liu, Xuan Di, Xianmao Lu, Jianping Meng, and Zhou Li**

Ultraviolet (UV) photodetectors have attracted extensive attention in various applications, including aerospace, optical communication, and fire warning. However, the intrinsic coupling of high responsivity and fast response as well as imperfect interface transmission impede the further improvement of UV photodetector. Here, a high-performance Au-decorated PbI_2/ZnO pn junction UV photodetector with a one-dimensional (1D) and two-dimensional (2D) interspersed structure is presented. The pyro-phototronic effect and energy band engineering effect from the localized pn junction generated by the layered p-type PbI_2 nanosheets along the *c*-axis of ZnO are coupled to modulate the separation and transport of photogenerated carriers. Furthermore, the localized surface plasmon resonance of Au nanoparticles produces transient thermal power to raise temperature fast to enhance pyroelectric current. The self-powered Au@PbI_2/ZnO photodetector displays a high responsivity of 0.21 A W^{-1}, excellent detectivity of 7.9×10^{12} Jones, and fast response/recovery time of 25/31 ms, under the illumination of 325 nm light with the power density of 0.08 μW cm^{-2}. This work offers an effective strategy for designing high-performance next-generation optoelectronic devices.

1. Introduction

Ultraviolet (UV) photodetectors, which can convert light into electrical signals, play a crucial role in aerospace detection, missile tracking, optical communications, and fire warning.[1–3] The third-generated wide bandgap semiconductors represented by ZnO,[4–6] GaN,[7,8] SiC,[9,10] Ga_2O_3,[11,12] and diamond,[13] which are promising choices for constructing the heterojunction UV photodetector owing to their suitable cut-off wavelength determined by their bandgap, high chemical stability, good thermal conductivity and high saturation electron drift speed.[14–16] Whereas the intrinsic limits of imperfect interfacial transportation impede the further improvement of high-performance photodetector.[17–19]

The two-dimensional (2D) materials, which have the approaching perfect surface and high carrier mobility within the plane, provide unprecedented flexibility for integration with other dimensional materials and band engineering regulation.[20–23] Various types of heterojunctions can be constructed by stacking them with different dimensions, generating extra properties that do not exist in individual 2D materials.[24] For example, a van der Waals semiconductors heterojunction of SnS and GeS demonstrates a low concentration of carrier composite sites and excellent transportation of photo-generated electron-hole pairs across the interface.[25]

The emerging 2D layered material, lead iodide (PbI_2), possesses a wide bandgap, atomic-level thickness, absence of dangling bonds, and high carrier mobility making it a promising candidate for high-performance photodetectors.[26,27] Several methods have been developed for the fabrication of PbI_2 nanosheets (NSs), including mechanical exfoliation,[28] physical vapor deposition (PVD),[29] and solution processing.[27,30] However, these approaches posed significant challenges in terms of process complexity and high cost.[30,31] In addition, they may lead to the generation of defects and contamination, resulting in a substantial increase in defect states and surface states. The presence of these interfacial states induces a pronounced Fermi pinning effect at the electrode contact interface, leading to the formation of high Schottky barriers that impede effective charge transfer

X. Zheng, X. Lu, Z. Li
College of Chemistry and Chemical Engineering
Guangxi University
Nanning530004, China

X. Zheng, M. Dong, Q. Li, Y. Liu, X. Di, X. Lu, J. Meng, Z. Li
Beijing Institute of Nanoenergy and Nanosystems
Chinese Academy of Sciences
Beijing101400, China
E-mail: mengjianping@binn.cas.cn; zli@binn.cas.cn

M. Dong, J. Meng
School of Nanoscience and Engineering
University of Chinese Academy of Sciences
Beijing100049, China

Q. Li
College of Materials Science and Opto-Electronic Technology
University of Chinese Academy of Sciences
Beijing100049, China

Y. Liu, X. Di
School of Engineering and Technology
China University of Geosciences (Beijing)
Beijing100083, China

The ORCID identification number(s) for the author(s) of this article can be found under https://doi.org/10.1002/adom.202303177

DOI: 10.1002/adom.202303177

and limit photodetection capabilities.[32,33] Ultrathin, high-quality PbI_2 NSs with good optical properties is realized by a simple solution method, which has the advantages of simplicity, rapidity, and high efficiency while meeting the requirements for large-scale production. It provides a new idea to reduce interfacial defects through material preparation.

Like other 2D materials, PbI_2, which has an atomical thickness or few-layer structure, has low absorption and limited photon utilization due to its weak light-matter interactions.[34,35] In contrast, nanowire array structure can trap UV light by multiple reflections and has high absorption.[36,37] The nature of easy fabrication, semiconducting behavior as well as piezoelectric and pyroelectric properties, endows the more attraction for ZnO nanowires (NWs) more attractive in the field of UV photodetector.[38–40] In addition, the high-speed channels along the *c*-axis of ZnO NWs ensure the pyro-phototronic effect, which combines the pyroelectric effect and photoexcitation to efficiently modulate the separation and transportation of photogenerated carriers at the interface during the photodetection process.[41,42] More importantly, when the ZnO NWs heterojunction configuration was constructed, the pyro-phototronic effect not only enhanced responsivity and detectivity but also reduced response/recovery time significantly.[16] The pyro-phototronic effect has been confirmed to significantly improve performance by directly modulating the energy band structure at the interface through temperature changes.[43,44] Systemic investigation about the Si-ZnO pn junction is conducted to demonstrate the influence of surface states and chopper frequency on the pyro-phototronic effect.[45] Besides, the power-density dependent pro-phototronic effect is also clarified in the Ag-ZnO Schottky junction.[46] Utilizing the flexibility of ultrathin Si, a flexible photodetector enhanced by the pyro-phototronic effect is designed to detect near-infrared light by near-infrared photothermal triggered pyroelectric potential.[47] To enhance the responsivity of photodetectors, Au nanoparticles are commonly employed to introduce localized surface plasmon resonance (LSPR) effects, thereby improving the absorption and scattering of incident light and enhancing the injection efficiency of hot electrons.[48]

Based on this concept, we report UV photodetectors based on pn junction constructed by ZnO NWs and ultrathin PbI_2 NSs by coupling the pyro-phototronic effect, LSPR and energy band engineering, which utilizes a ZnO NWs as a photoactive channel, and PbI_2 NSs as a gain layer. The type-II band alignment of PbI_2 and ZnO facilitates effective spatial separation of photocarriers with photogenerated holes being captured in PbI_2, while electrons undergo in ZnO NWs, resulting in high photocurrent. Furthermore, the coupling of pyro-phototronic effects, energy band engineering, and hole-trapping effect achieve ultra-sensitive detection of UV light at low power density. These synergetic effects endow the Au@PbI_2/ZnO device to display excellent performance at zero bias, including the high responsivity of 0.21 A W^{-1}, fast response/recovery time (25/31 ms), high detectivity of 7.9×10^{12} Jones. Our work provides an approach to design the high-performance photodetector for the hybrid heterojunction by coupling energy band engineering and LSPR effects, and it will be able to offer new thoughts on the next-generation optoelectronic devices.

2. Result and Discussion

The illustration and structural characterizations of the self-powered Au@PbI_2/ZnO pn junction photodetector are shown in **Figure 1**. The ZnO NWs are grown vertically along the *c*-axis on FTO, while the PbI_2 NSs are fabricated using a facile solution processing method (Figure S1, Supporting Information). The horizontally aligned PbI_2 NSs evenly in situ grown on the surface of ZnO NWs, forming a 1D and 2D interspersed structure (Figure 1a). This structure not only facilitates the transportation of photo-generated carriers as well as light absorption but also provides strong interfacial interaction between PbI_2 and ZnO. Furthermore, the localized pn junctions formed on the side surfaces of ZnO NWs would result in band bending and electron-depleted surfaces, benefiting the separation of photo-generated electron-hole pairs and suppression of dark current. The SEM image clearly reveals the distinct features of PbI_2 NSs and their interspersed structure (Figure 1b and Figure S2). TEM images further confirm this structure, showing distinct stacking of PbI_2 NSs on the ZnO NWs (Figure 1c). Moreover, HRTEM analysis demonstrates the presence of PbI_2 by measuring interplanar spacing, which closely matches that of (003) planes in PbI_2 (enlarged image in Figure 1c). XRD patterns obtained from the array of ZnO NWs covered with PbI_2 NSs verify the phase identification of both materials (Figure 1d), where prominent diffraction peaks corresponding to (001) and (002) crystal planes can be assigned to PbI_2 and ZnO, respectively. As shown in Figure 1e, significant absorption is observed for both ZnO NWs and PbI_2 NSs. Furthermore, the bandgap of ZnO and PbI_2 can be determined as 3.73 and 2.36 eV, respectively (Figure S1, Supporting Information).

Figure 2a compares the photoelectron transition in direct and indirect bandgap semiconductors. In a direct-bandgap semiconductor, electron transitions occur within the same momentum space from the valence band maximum (V_{BM}) to the conduction band minimum (C_{BM}). However, in indirect-bandgap semiconductors, generation, and recombination processes involve phonon-assisted absorption and emission.[49,50] The photogeneration rates of direct-bandgap semiconductors are significantly higher than those of indirect-bandgap semiconductors, indicating their superior suitability for photodetection applications.[51] Both ZnO and PbI_2 exhibit direct bandgaps, benefiting for constructing high-performance photodetectors.[52] Figure 2b provides a concise illustration of the energy band diagram for these materials, depicting their valence bands, conduction bands, and vacuum energy levels. The appropriate band alignment of the device ensures that electrons are injected from the photoexcited layer of PbI_2 and ZnO and collected by the FTO electrode, while holes in the valence band reach the Ag electrode through the hole transport layer. The Schottky barrier heights between Ag and PbI_2 determine carrier transport across the metal-semiconductor interface and influence device performance. To investigate photogenerated charge separation and transport behavior, Kevin-probe force microscopy (KPFM) tests were conducted to visualize the surface potential of PbI_2 and Ag (Figure 2c,e).[53] This result implies a preferential flow of photogenerated holes from PbI_2 to Ag (Details in Note S2, Supporting Information). Figure 2f is the equivalent circuit diagram. The photo-generated current can easily pass through the PbI_2 and Ag interfaces (Figure *I*–*V* charac-

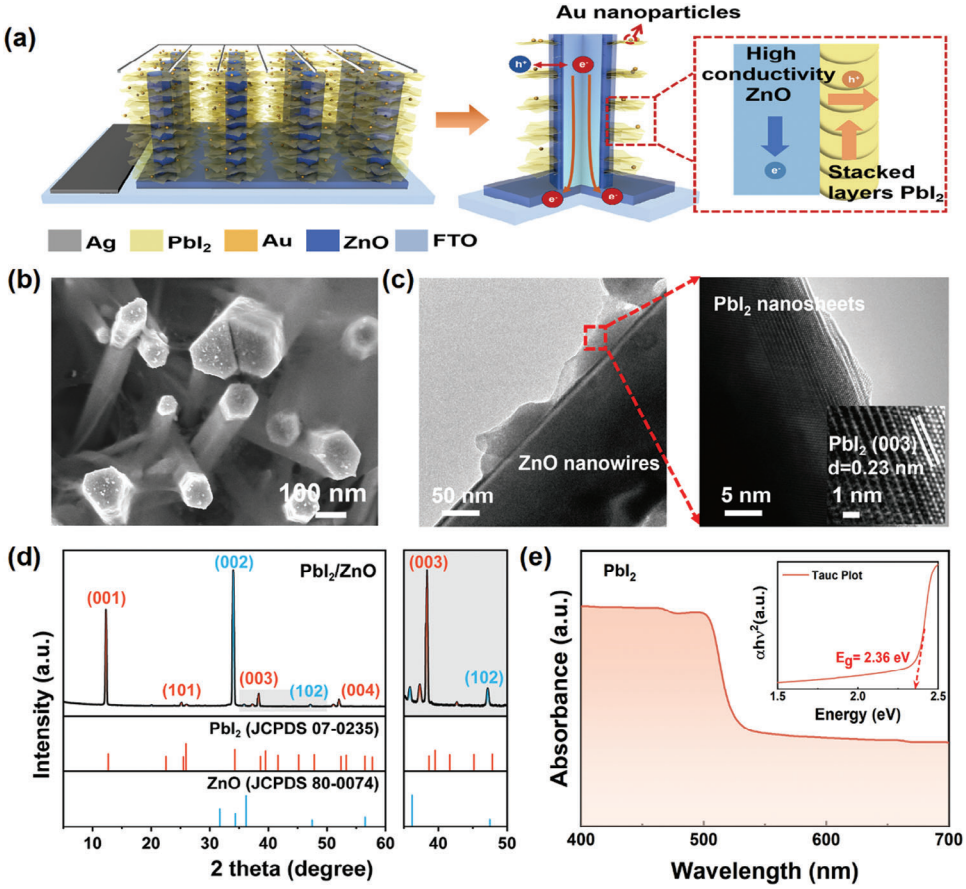

Figure 1. Illustration and structural characterizations of Self-powered Au@PbI_2/ZnO pn junction photodetectors. a) Schematic demonstration of the structure of self-powered photodetectors. Ag interdigital electrode acts as carrier collector. b) Scanning electron microscope (SEM) images of the heterojunction. c) The TEM and HRTEM image of PbI_2/ZnO heterojunction. d) XRD pattern of PbI_2/ZnO heterojunction. e) UV–vis absorption spectrums of PbI_2 nanosheets. Insert: Tauc-Plot.

teristics of the self-powered Au@PbI_2/ZnO photodetector under 325 nm illumination (red curve in Figure 2g) were measured and compared with dark current (blue curve in Figure 2g), showing excellent ultraviolet response. Self-powered operations are observed from enlarged *I–V* curves (Figure 2h), showing a measurable photocurrent (1.18 μA) under UV illumination at zero bias. This can be attributed to the well-aligned band structure of the device.

Comprehensive characterizations of the photoelectric properties are conducted for the self-powered Au@PbI_2/ZnO photodetector. In order to systematically investigate the figures of merit, we performed measurements under 325 nm illumination to represent its photodetection capability. The dynamic photo-response of the self-powered device is evaluated at various power intensities (**Figure** 3a). As the power density increases, the transient photocurrent of the device is enhanced. The obvious phenomenon that pyroelectric current is gradually decreased at a high power density of 1.62 and 3.23 μW cm^{-2} is noticeable. Pyroelectric current is dependent on the temperature change of the material. At the initial state, the temperature change is huge because the materials keep the low temperature. Then, the temperature of materials is increased after multiple illuminations, which decreases the temperature change and pyroelectric current slightly.[42,54,55]

In terms of time parameters, the response time (τ) refers to the duration required for the output current of the photodetector to reach a stable response value or return to its pre-irradiation level. The rise time (τ_r) refers to the duration time required for photocurrent to increase from 10% to 90%, while the fall time (τ_f) represents the duration time for the photocurrent to decrease from 90% to 10%.[56] Consequently, the calculated rise/fall time is merely 25/31 ms, which is believed to be associated with the efficient separation and transportation of photo-generated electron-hole pairs facilitated by both the built-in potential in pn junction and transient pyro-potential resulting from the light-induced changes in spontaneous polarization (Figure 3b). To further evaluate the performance of the heterojunction, two additional key parameters are considered: responsivity (R) and detectivity (D^*). Responsivity (R) defined as the ratio of photocurrent or photovoltage of the photodetector to the incident light power. It can be calculated as $R = (I_{light} - I_{dark})/(AP_\lambda)$, where I_{light} is the photocurrent and I_{dark} is the dark current, $P_\lambda$and A are the optical power density and the effective area of the photodetectors, respectively. D^* is introduced to evaluate the ability of a device to detect weak light signals, which defined as $D^* = R/(2eI_{dark})^{1/2}$. Among them, R is the responsivity and e is the electron charge. As depicted in Figure 3c,d, the maximum value of R and D* are

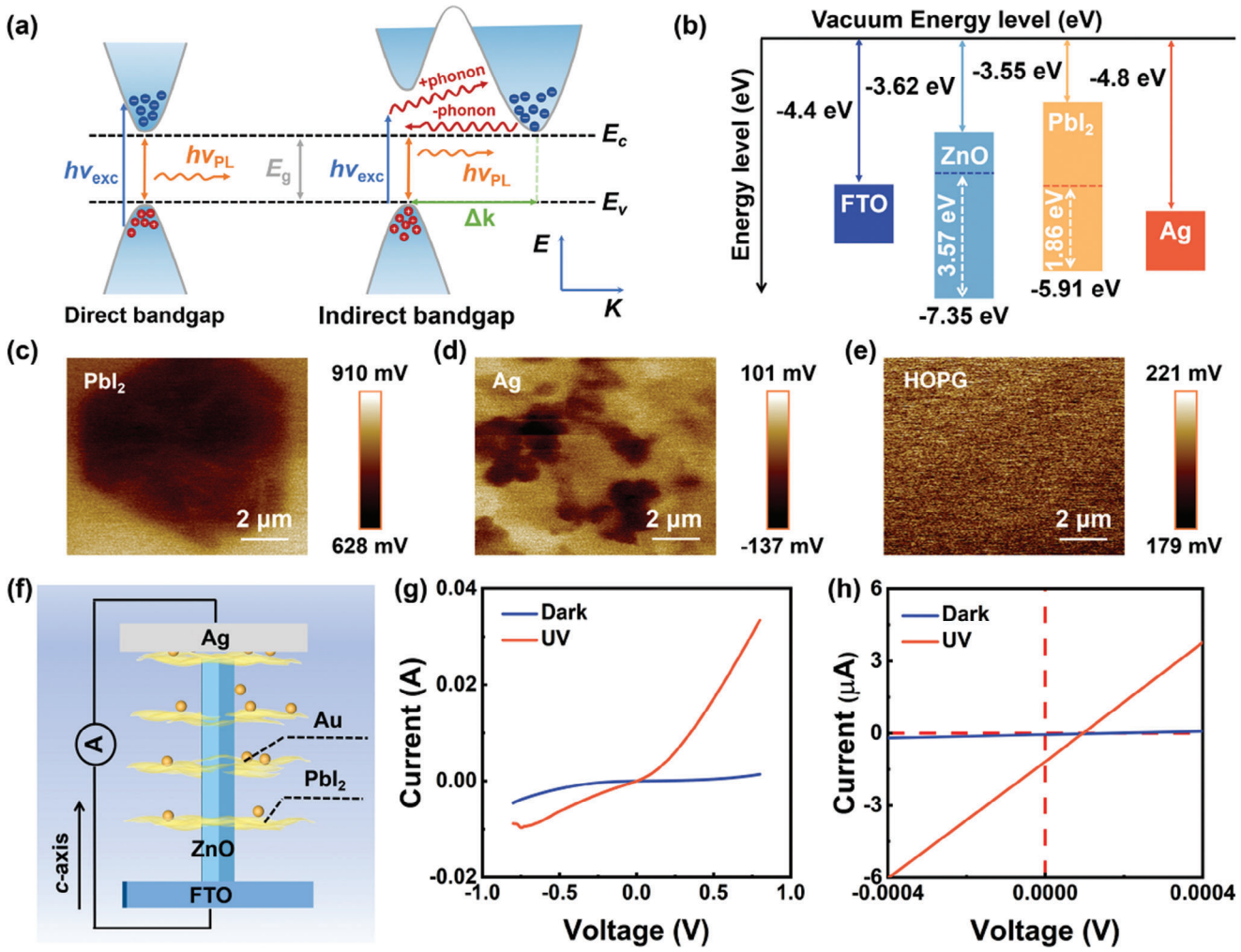

Figure 2. Energy band structure and electrical measurements. a) Photoelectron transition in direct and indirect bandgap semiconductors. b) Energy band diagram of FTO, ZnO, PbI_2, Ag. Potential images of c) PbI_2, d) Ag, and e) HOPG obtained by KPFM. f) The schematic diagram of the contact interface for Ag and PbI_2. g) *I–V* characteristics of the self-powered Au@PbI_2/ZnO photodetectors under dark and 325 nm laser illumination. h) partial enlargement of *I–V* curve.

0.21 A W^{-1} and 7.9×10^{12} Jones, respectively, at the power intensity of 0.08 μW cm^{-2}. Furthermore, external quantum efficiency (EQE), which is directly proportional to the responsivity, represents the ratio of collected electrons by the contact to injected photons.[56] Therefore, EQE can be expressed as $EQE = Rhc/e\lambda$, where h is the Planck constant and λ is the wavelength of the incidence light. The high EQE of 80% for the Au@PbI_2/ZnO photodetector at zero bias is presented in Figure 3e, which can be attributed to the free-barrier band transport and detection-free interfaces. The corresponding photocurrents (I_{light}) are extracted and plotted in Figure 3f. It is evident that photocurrent (I_{light}) monotonically increases with the power density (P_λ) of illumination following the equation of $I = C \cdot P^\beta$, where C is a constant, P is the incident power density, and β is the light intensity exponent extracted from the power-law relation.[57] The calculated value of β is 0.60, showing significant photocurrent and excellent linearity in Figure 3f. The sublinear behavior suggests the presence of trap centers in the channel materials, which can induce photo-gain. Under lower power conditions, most of these trap states (of the minority carrier) become filled. Consequently, further increasing light power cannot effectively enhance photo gain but instead leads to increased recombination probability, resulting in a decrease in responsivity.[58] We attribute the high value of β to the higher crystallinity and reduced defect density, indicating significant improvements in both detectivity and responsivity through the pyro-phototronic effect and LSPR effect. Furthermore, the performance superiority of the Au@PbI_2/ZnO device is comparable to or even surpass most previously reported ZnO-based photodetectors at zero bias. As shown in Figure 3g and Table S1 (Supporting Information), the advantage of responsivity and detectivity was displayed compared to the previous works.

The working mechanism of the Au@PbI_2/ZnO photodetectors is depicted in **Figure 4**. Figure 4a illustrates the formation of a pn junction at the interface between PbI_2 and ZnO, resulting in an upward bending of the energy band around the interface. Additionally, the energy band is cyclic bending along the c-axis of ZnO due to the localized pn junction generated by the layered p-type PbI_2 NSs. These grain boundaries can act

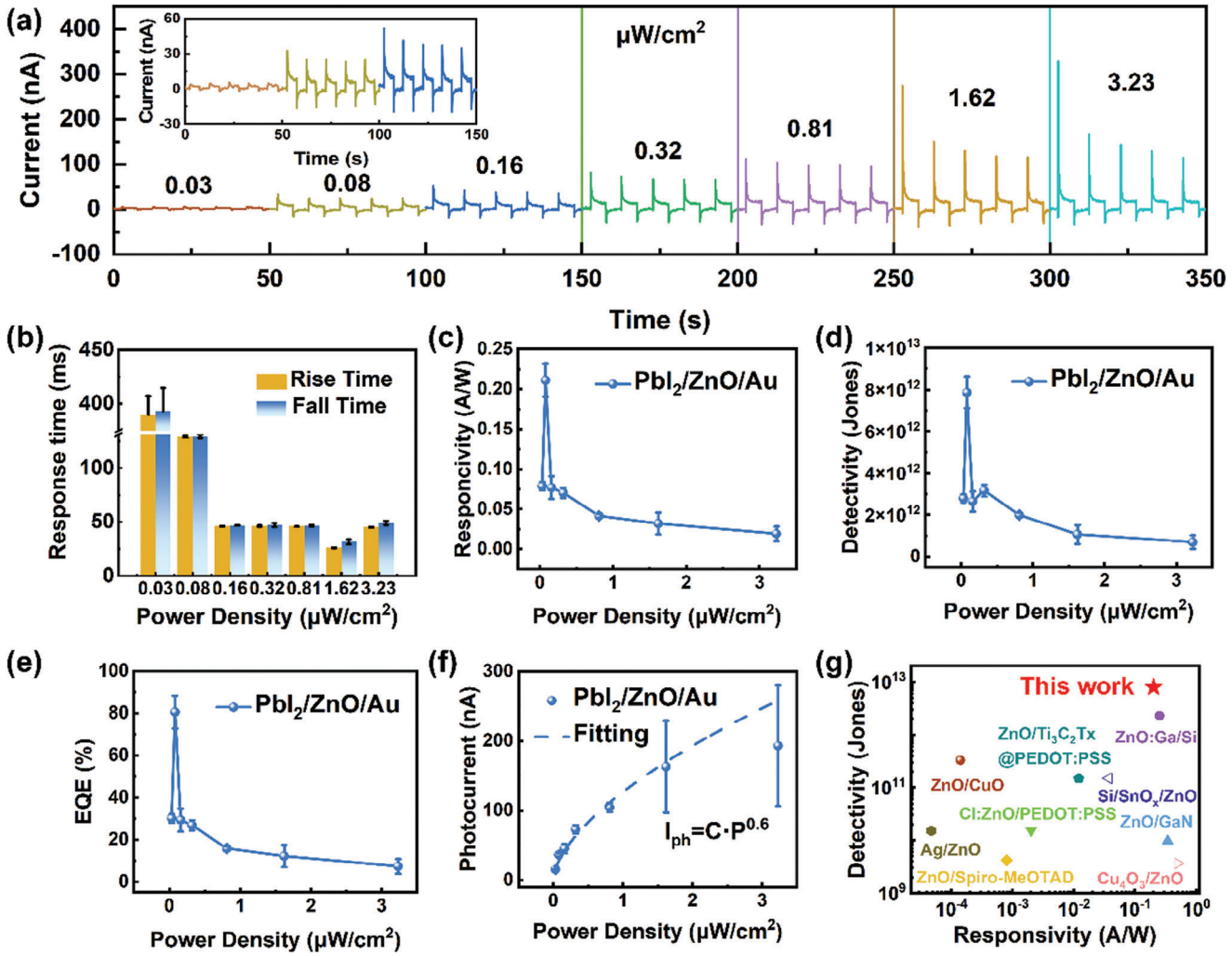

Figure 3. Pyroelectric effect enhanced performances of self-powered devices. a) I–t characteristics of self-powered Au@PbI_2/ZnO photodetectors under 325 nm illuminations with different power densities from 0.03 to 3.23 μW cm^{-2}, the insert is the enlarged I–t curves under the corresponding illumination conditions. Variation of b) response time, c) responsivity, d) detectivity, e) EQE and f) photocurrent of device with the incident optical power density. g) Comparison of, D^* for our device with previous reports on self-powered ZnO-based photodetectors at zero bias. References are shown in Table S1 (Supporting Information).

as energy barriers to carrier transport in dark conditions and introduce additional band-edge modulation along the *c*-axis of the ZnO.[59] Once the 325 nm light illumination, the valence band electrons are excited to the conduction band, generating electron-hole pairs. These holes are then trapped at the trap location of energy band bending. Additionally, the presence of Au nanoparticles induces LSPR, leading to rapid temperature changes within picosecond durations upon illumination. These temperature fluctuations give rise to a transient pyroelectric potential along the *c*-axis and enhance the pyro-phototronic effect, forming a negative charge at the interface of the Au@PbI_2/ZnO heterojunction. Consequently, the energy band bends upward, reducing the barrier height of the pn junction and facilitating peak current generation. Additionally, higher energy plasmonic hot electrons could overcome the energy barrier at the interface, which could be confined in the conduction band of ZnO and enhance the photo-response performance of devices. The Schottky junction of Au NPs and ZnO and the localized p-n junction of PbI_2/ZnO would reduce the electrons in the ZnO NWs due to the formation of depletion region along the *c*-axis of ZnO, weaken the potential screening effect on the pyro-polarization charges and enhance the pyroelectric current. Moreover, the localized energy band bending would lead to more difficult electron transport near the surface and prolong the lifetime of photogenerated electron-hole pairs. This phenomenon has been demonstrated in a previous report (Figure 4b). Even under continuous irradiation of 325 nm light, the pyroelectric potential disappears of *c*-axis ZnO NWs owing to realizing heat balance. The photocurrent response decreases significantly and eventually reaches a steady state (Figure 4c). When the light is turned off, a reverse pyroelectric potential is generated at the pn junction of the photodetector, which pushes the valence band downwards and increases the height of the barrier at the interface. Meanwhile, a strong reverse current is observed due to the reverse thermoelectric charge

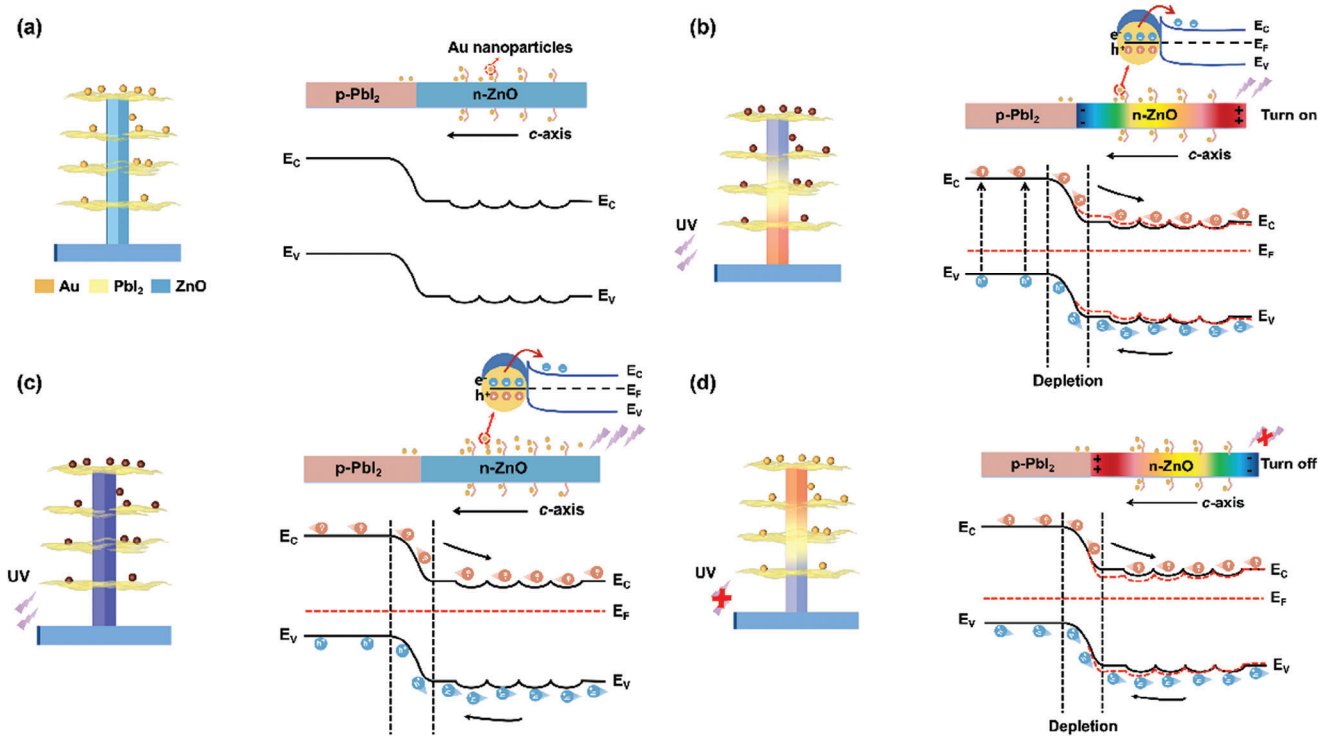

Figure 4. The working mechanism of self-powered Au@PbI_2/ZnO heterojunction combined with energy band engineering and LSPR-enhanced pyro-phototronic effect. a) Energy band diagram of Au@PbI_2/ZnO heterojunction in the absence of light. b) Energy band diagram of Au@PbI_2/ZnO heterojunction at the moment of light illumination. c) Energy band diagram of Au@PbI_2/ZnO heterojunction under continuous illumination. d) Band diagram of Au@PbI_2/ZnO heterojunction once the light is turned off.

caused by the instantaneous temperature decrease. Finally, in the absence of laser irradiation, the device cools down to room temperature and remains stable, and the output current returns to the dark current as the pyroelectric current decays (Figure 4d).

3. Conclusion

In summary, we design and prepare Au@PbI_2/ZnO pn junction with a hybrid dimensional interspersed structure and demonstrate a high-performance UV photodetector via the energy band engineering and LSPR effect. The self-powered UV photodetector not only exhibits the excellent properties of charge separation and transport but also endows the superiority of interface charge collection. More importantly, the unique band edge modulation from the localized pn junction generated by the layered p-type PbI_2 NSs along the *c*-axis of ZnO and its pyro-phototronic effect, which enhances the separation and transportation of photogenerated electron-hole pairs. The optimized self-powered Au@PbI_2/ZnO photodetector exhibits superior comprehensive performance with a high responsivity of 0.21 A W^{-1}, excellent detectivity of 7.9×10^{12} Jones, response/recovery time of 25/31 ms, even if it is illuminated by UV light with the power density of 0.08 μW cm^{-2}. This work provides a universal strategy for developing high-performance photodetectors through coupling energy band engineering and LSPR effect, and it will be able to offer new thoughts on the next-generation optoelectronic devices.

4. Experimental Section

Synthesis of ZnO NWs: ZnO NWs were synthesized using the hydrothermal method, following a previously reported method. First, FTO glasses were ultrasonically cleaned for 15 min in acetone and ethanol, followed by distilled water rinsing. Subsequently, a thin seed layer of ZnO NWs was deposited on the FTO glasses using radio frequency magnetron sputtering (Denton Discovery 635). The substrate with the seed layer was then immersed into mixed nutrient solutions for ZnO NWs growth at 95 °C for 4 h. The solution contained H_2O, 5 M Zn $(NO_3)_2 \cdot 6H_2O$, 5 M HMTA, and ammonium hydroxide. Finally, the products were thoroughly cleaned with ethanol and distilled water before being collected and vacuum-dried at 70 °C.

Preparation of PbI_2/ZnO Heterojunction: The synthesized PbI_2 powder was mixed in deionized water at 150 °C for 1 h. Next, the concentration of 4 mg mL^{-1} PbI_2 solution was prepared for further usage. PbI_2 solution was spin-coated on the plasma-cleaned ZnO NWs array at 100 rpm. Finally, heat it at 60 °C for 20 min.

Fabrication Process of Au@PbI_2/ZnO Photodetectors: Ag interdigitated electrodes are covered on the top of the functional materials, with an electrode distance is 2 mm. Testing wires were connected to the top and bottom electrodes by silver paste. Then, a thin layer of Kapton tape was employed to fix the testing wires, with the purpose of improving their resistance to environmental contaminations and corrosions. Finally, Au nanoparticles were attached to the surface of the material by 10^8 Auto Cressington sputter coater with 10 mA current for 120 s. The device sizes are 1.5 cm × 2 cm.

Material Characterizations: The detailed microscopic structures and morphology of ZnO NWs arrays, PbI_2 NSs, and PbI_2-ZnO heterojunctions were characterized by using SEM (Hitachi SU8020), TEM (Tecnai G F20 TWIN UEM), and corresponding EDS. The composition of the material was measured on X-ray diffractometer (PANalytical X'Pert) with

monochromatized Cu Kα radiation (λ = 1.5406 Å). Absorption spectra were collected by Shimadzu UV3600 at room temperature.

Electrical and Optical Measurements: The *I–V* characteristics were measured by the Keithley Semiconductor Characterization System (Model 4200-SCS). The voltage between −0.8 V and +0.8 V was applied on the device. The optical input stimuli were provided by a monochromatic 325 nm laser (LabRAM HR Evolution, Horiba). A continuously variable attenuator was used to change the light power density in the Raman System. The corresponding light power density was measured by digital power meters (THORLBS PM100D, Dachau Germany). I-t data was measured and recorded by a LeCroy oscilloscope and a Keithley 6517B high-resistance electrometer. The area of UV illumination covered the whole photodetector. The interactive area between UV light and photodetectors is 2 cm × 1.5 cm.

Supporting Information

Supporting Information is available from the Wiley Online Library or from the author.

Acknowledgements

The authors are thankful for the support provided by the National Natural Science Foundation of China (Grant No. 52002027, T2125003), the Youth Innovation Promotion Association CAS (Grant No. 2023175), the China Postdoctoral Science Foundation (Grant No. 119103S433), and the Fundamental Research Funds for the Central Univeristies (Grant No. E3E41806X2).

Conflict of Interest

The authors declare no conflict of interest.

Data Availability Statement

Research data are not shared.

Keywords

energy band engineering, LSPR, pyro-phototronic effect, self-powered, UV photodetectors

Received: December 25, 2023
Published online:

[1] J. Liu, F. Xia, D. Xiao, F. J. García De Abajo, D. Sun, *Nat. Mater.* **2020**, *19*, 830.
[2] Z. Zhao, C. Xu, Y. Ma, K. Yang, M. Liu, X. Zhu, Z. Zhou, L. Shen, G. Yuan, F. Zhang, *Adv. Funct. Mater.* **2022**, *32*, 2203606.
[3] Q. Li, Z. Li, J. Meng, *Int. J Optomechatroni.* **2022**, *16*, 1.
[4] Y. Zhang, M. Hu, Z. Wang, *Nano Energy* **2020**, *71*, 104630.
[5] H. Yu, Q. Liao, Z. Kang, Z. Wang, B. Liu, X. Zhang, J. Du, Y. Ou, M. Hong, J. Xiao, Z. Zhang, Y. Zhang, *Small* **2020**, *16*, 2005520.
[6] Q. Li, J. Meng, J. Huang, Z. Li, *Adv. Funct. Mater.* **2022**, *32*, 2108903.
[7] Y. Han, Y. Wang, S. Fu, J. Ma, H. Xu, B. Li, Y. Liu, *Small* **2023**, *19*, 2206664.
[8] T. Hu, L. Zhao, Y. Wang, H. Lin, S. Xie, Y. Hu, C. Liu, W. Zhu, Z. Wei, J. Liu, K. Wang, *ACS Nano* **2023**, *17*, 8411.
[9] Y. Zhang, Y.-C. Wang, L. Wang, L. Zhu, Z. L. Wang, *Adv. Mater.* **2022**, *34*, 2204363.
[10] J. Hu, X. Wang, L. Lin, J. Xu, M. Liu, R. Wang, X. Li, L. Tao, Y. Sui, B. Song, *ACS Appl. Mater. Interfaces* **2023**, *15*, 1505.
[11] Q. Zhang, N. Li, T. Zhang, D. Dong, Y. Yang, Y. Wang, Z. Dong, J. Shen, T. Zhou, Y. Liang, W. Tang, Z. Wu, Y. Zhang, J. Hao, *Nat. Commun.* **2023**, *14*, 418.
[12] M. Ding, K. Liang, S. Yu, X. Zhao, H. Ren, B. Zhu, X. Hou, Z. Wang, P. Tan, H. Huang, Z. Zhang, X. Ma, G. Xu, S. Long, *Adv. Optical Mater.* **2022**, *10*, 2200512.
[13] B. Liu, K. Liu, S. Zhang, V. G. Ralchenko, X. Zhang, J. Xue, D. Wen, P. Qiao, J. Zhao, B. Dai, L. Yang, J. Han, J. Zhu, *ACS Appl. Electron. Mater.* **2022**, *4*, 5996.
[14] Y. Wang, L. Li, H. Wang, L. Su, H. Chen, W. Bian, J. Ma, B. Li, Z. Liu, A. Shen, *Nanoscale* **2020**, *12*, 1406.
[15] J. Meng, Q. Li, J. Huang, C. Pan, Z. Li, *Nano Today* **2022**, *43*, 101399.
[16] Q. Li, J. Huang, J. Meng, Z. Li, *Adv. Optical Mater.* **2022**, *10*, 2102468.
[17] Y. Niu, X. Zhou, W. Gao, M. Fu, Y. Duan, J. Yao, B. Wang, M. Yang, Z. Zheng, J. Li, *ACS Nano* **2023**, *17*, 13760.
[18] G. Kwon, Y.-H. Choi, H. Lee, H.-S. Kim, J. Jeong, K. Jeong, M. Baik, H. Kwon, J. Ahn, E. Lee, M.-H. Cho, *Nat. Electron.* **2022**, *5*, 241.
[19] J. Meng, Q. Li, J. Huang, Z. Li, *Nanoscale* **2021**, *13*, 17101.
[20] H.-Z. Zhang, W.-J. Wu, L. Zhou, Z. Wu, J. Zhu, *Small Sci.* **2022**, *2*, 2100033.
[21] T. Ma, H. Chen, K. Yananose, X. Zhou, L. Wang, R. Li, Z. Zhu, Z. Wu, Q.-H. Xu, J. Yu, C. W. Qiu, A. Stroppa, K. P. Loh, *Nat. Commun.* **2022**, *13*, 5465.
[22] M. Turunen, M. Brotons-Gisbert, Y. Dai, Y. Wang, E. Scerri, C. Bonato, K. D. Jöns, Z. Sun, B. D. Gerardot, *Nat. Rev. Phys.* **2022**, *4*, 219.
[23] Q. Li, J. Meng, Z. Li, *J. Mater. Chem. A* **2022**, *10*, 8107.
[24] X. Yu, X. Wang, F. Zhou, J. Qu, J. Song, *Adv. Funct. Mater.* **2021**, *31*, 2104260.
[25] E. Sutter, R. R. Unocic, J.-C. Idrobo, P. Sutter, *Adv. Sci.* **2022**, *9*, 2103830.
[26] C. Cong, J. Shang, L. Niu, L. Wu, Y. Chen, C. Zou, S. Feng, Z.-J. Qiu, L. Hu, P. Tian, Z. Liu, T. Yu, R. Liu, *Adv. Optical Mater.* **2017**, *5*, 1700609.
[27] Y. Sun, Z. Zhou, Z. Huang, J. Wu, L. Zhou, Y. Cheng, J. Liu, C. Zhu, M. Yu, P. Yu, W. Zhu, Y. Liu, J. Zhou, B. Liu, H. Xie, Y. Cao, H. Li, X. Wang, K. Liu, X. Wang, J. Wang, L. Wang, W. Huang, *Adv. Mater.* **2019**, *31*, 1806562.
[28] P. Wangyang, H. Sun, X. Zhu, D. Yang, X. Gao, *Mater. Lett.* **2016**, *168*, 68.
[29] M. Zhong, L. Huang, H.-X. Deng, X. Wang, B. Li, Z. Wei, J. Li, *J. Mater. Chem. C* **2016**, *4*, 6492.
[30] W. Zheng, Z. Zhang, R. Lin, K. Xu, J. He, F. Huang, *Adv. Electron. Mater.* **2016**, *2*, 1600291.
[31] J. Liu, Y. Xue, Z. Wang, Z.-Q. Xu, C. Zheng, B. Weber, J. Song, Y. Wang, Y. Lu, Y. Zhang, Q. Bao, *ACS Nano* **2016**, *10*, 3536.
[32] J. Ma, H. Chi, A. Wang, P. Wang, H. Jing, T. Yao, C. Li, *J. Am. Chem. Soc.* **2022**, *144*, 17540.
[33] J. Jang, H.-S. Ra, J. Ahn, T. W. Kim, S. H. Song, S. Park, T. Taniguch, K. Watanabe, K. Lee, D. K. Hwang, *Adv. Mater.* **2022**, *34*, 2109899.
[34] T. Tong, Y. Gan, W. Li, W. Zhang, H. Song, H. Zhang, K. Liao, J. Deng, S. Li, Z. Xing, Y. Yu, Y. Tu, W. Wang, J. Chen, J. Zhou, X. Song, L. Zhang, X. Wang, S. Qin, Y. Shi, W. Huang, L. Wang, *ACS Nano* **2023**, *17*, 530.
[35] Y. Sun, Y. Sun, R. Wang, K. Liu, *Prog. Nat. Sci.: Mater. Int.* **2022**, *32*, 528.
[36] J. Mao, B. Zhang, Y. Shi, X. Wu, Y. He, D. Wu, J. Jie, C.-S. Lee, X. Zhang, *Adv. Funct. Mater.* **2022**, *32*, 2108174.
[37] T. S. Vo, T. T. B. C. Vo, *Prog. Nat. Sci.: Mater. Int.* **2022**, *32*, 314.
[38] S. Sahare, P. Ghoderao, M. K. Sharma, M. Solovan, R. Aepuru, M. Kumar, Y. Chan, M. Ziółek, S.-L. Lee, Z.-H. Lin, *Nano Energy* **2023**, *107*, 108172.
[39] J. Huang, Q. Li, X. Lu, J. Meng, Z. Li, *Adv. Mater. Interfaces* **2022**, *9*, 2200327.

[40] A. Kem, K. S. Pasupuleti, M. Jayasimhadri, M.-D. Kim, K. R. Peta, *J. Alloys Compd.* **2023**, *960*, 170841.
[41] Y. Zhang, L. Yang, Y. Zhang, Z. Ding, M. Wu, Y. Zhou, C. Diao, H. Zheng, X. Wang, Z. L. Wang, *ACS Nano* **2020**, *14*, 10723.
[42] Y. Wang, L. Zhu, Y. Feng, Z. Wang, Z. L. Wang, *Adv. Funct. Mater.* **2019**, *29*, 1807111.
[43] K. S. Pasupuleti, M. Reddeppa, B.-G. Park, K. R. Peta, J.-E. Oh, S.-G. Kim, M.-D. Kim, *ACS Appl. Mater. Interfaces* **2020**, *12*, 54181.
[44] M. Reddeppa, B.-G. Park, K. S. Pasupuleti, D.-J. Nam, S.-G. Kim, J.-E. Oh, M.-D. Kim, *Semicond. Sci. Technol.* **2021**, *36*, 035010.
[45] Y. Feng, Y. Zhang, Y. Wang, Z. Wang, *Nano Energy* **2018**, *54*, 429.
[46] Y. Wang, J. Sun, T. Jiang, C. Yang, Q. Tan, S. Guo, Y. Liu, *Mater. Sci. Eng. A* **2019**, *754*, 1.
[47] L. Chen, J. Dong, M. He, X. Wang, *Beilstein J. Nanotechnol.* **2020**, *11*, 1623.
[48] Y. Zhu, B. Wang, C. Deng, Y. Wang, X. Wang, *Nano Energy* **2021**, *83*, 105801.
[49] B. Yang, X. Mao, F. Hong, W. Meng, Y. Tang, X. Xia, S. Yang, W. Deng, K. Han, *J. Am. Chem. Soc.* **2018**, *140*, 17001.
[50] D. Gelija, C. Loka, M. Goddati, N.-H. Bak, J. Lee, M.-D. Kim, *ACS Appl. Mater. Interfaces* **2023**, *15*, 34883.
[51] L. Mei, R. Huang, C. Shen, J. Hu, P. Wang, Z. Xu, Z. Huang, L. Zhu, *Adv. Opt. Mater.* **2022**, *10*, 2102656.
[52] S. Liu, M.-Y. Li, J. Zhang, D. Su, Z. Huang, S. Kunwar, J. Lee, *Nano-Micro Lett.* **2020**, *12*, 114.
[53] L. Mei, K. Zhang, N. Cui, W. Yu, Y. Li, K. Gong, H. Li, N. Fu, J. Yuan, H. Mu, Z. Huang, Z. Xu, S. Lin, L. Zhu, *Small* **2023**, *19*, 2301386.
[54] L. Li, D. Zheng, Y. Xiong, C. Yu, H. Yin, X. Yu, *RSC Adv.* **2022**, *12*, 35341.
[55] Z. Li, C. Ji, Y. Fan, T. Zhu, S. You, J. Wu, R. Li, Z.-K. Zhu, P. Yu, X. Kuang, J. Luo, *J. Am. Chem. Soc.* **2023**, *145*, 25134.
[56] F. Wang, T. Zhang, R. Xie, Z. Wang, W. Hu, *Nat. Commun.* **2023**, *14*, 2224.
[57] W. He, L. Kong, P. Yu, G. Yang, *Adv. Mater.* **2023**, *35*, 2209995.
[58] S. Ghosh, A. Varghese, K. Thakar, S. Dhara, S. Lodha, *Nat. Commun.* **2021**, *12*, 3336.
[59] X. Liu, L. Gu, Q. Zhang, J. Wu, Y. Long, Z. Fan, *Nat. Commun.* **2014**, *5*, 4007.